AFRL-AFOSR-VA-TR-2023-0216

Weyl Fermion Devices for Chipscale Communications

Kolodzey, James
UNIVERSITY OF DELAWARE
220 HULLIHEN HALL
NEWARK, DE, 19716
USA

11/30/2022
Final Technical Report

Air Force Research Laboratory
Air Force Office of Scientific Research
Arlington, Virginia 22203
Air Force Materiel Command

REPORT DOCUMENTATION PAGE

PLEASE DO NOT RETURN YOUR FORM TO THE ABOVE ORGANIZATION.

1. REPORT DATE	2. REPORT TYPE	3. DATES COVERED	
20221130	Final	START DATE 20170201	END DATE 20210630

4. TITLE AND SUBTITLE
Weyl Fermion Devices for Chipscale Communications

5a. CONTRACT NUMBER	5b. GRANT NUMBER	5c. PROGRAM ELEMENT NUMBER
	FA9550-17-1-0134	61102F
5d. PROJECT NUMBER	**5e. TASK NUMBER**	**5f. WORK UNIT NUMBER**

6. AUTHOR(S)
James Kolodzey

7. PERFORMING ORGANIZATION NAME(S) AND ADDRESS(ES)
UNIVERSITY OF DELAWARE
220 HULLIHEN HALL
NEWARK, DE 19716
USA

8. PERFORMING ORGANIZATION REPORT NUMBER

9. SPONSORING/MONITORING AGENCY NAME(S) AND ADDRESS(ES)	10. SPONSOR/MONITOR'S ACRONYM(S)	11. SPONSOR/MONITOR'S REPORT NUMBER(S)
Air Force Office of Scientific Research 875 N. Randolph St. Room 3112 Arlington, VA 22203	AFRL/AFOSR RTB1	AFRL-AFOSR-VA-TR-2023-0216

12. DISTRIBUTION/AVAILABILITY STATEMENT
A Distribution Unlimited: PB Public Release

13. SUPPLEMENTARY NOTES

14. ABSTRACT
During the fourth year of this research program, investigations continued on multiterminal devices fabricated from semimetals with near-zero energy bandgap to study the possibility of Weyl fermion-effects on their operation and performance. With their exotic, topologically protected properties, Weyl fermion devices may produce electronic and optical circuits with ultra-high speeds and ultra-low power (dissipationless) drain, with operation at far-infrared wavelengths. Work continued on the Weyl semimetals MoTe2 and WTe2, as well as on lowenergy bandgap GeSn alloys, which were hoped to have Weyl-like behavior. The infrared photoresponse of multi-terminal devices was measured at wavelengths near 10 micrometers. It was found that these devices had interesting polarization-dependent photoresponse and could distinguish the incident polarization including circular from horizontal and vertical linear polarization.

15. SUBJECT TERMS

16. SECURITY CLASSIFICATION OF:			17. LIMITATION OF ABSTRACT	18. NUMBER OF PAGES
a. REPORT U	b. ABSTRACT U	c. THIS PAGE U	UU	16

19a. NAME OF RESPONSIBLE PERSON	19b. PHONE NUMBER *(Include area code)*
GERNOT POMRENKE	426-8426

Weyl Fermion Devices for Chipscale Communications

Fourth Annual Report to the Air Force Office of Science and Research:

Period of Performance for this Report : 2/1/20 – 9/30/21

PI: Prof. James Kolodzey, University of Delaware
Award No.: FA9550-17-1-0134
Award Dates: 01 Feb 2017 – 30 Sept 2021
AFOSR Program Manager: Dr. Gernot Pomrenke

Table of Contents

Abstract

During the fourth year of this research program, investigations continued on multiterminal devices fabricated from semimetals with near-zero energy bandgap to study the possibility of Weyl fermion-effects on their operation and performance. With their exotic, topologically protected properties, Weyl fermion devices may produce electronic and optical circuits with ultra-high speeds and ultra-low power (dissipationless) drain, with operation at far-infrared wavelengths. Work continued on the Weyl semimetals $MoTe_2$ and WTe_2, as well as on low-energy bandgap GeSn alloys, which were hoped to have Weyl-like behavior. The infrared photoresponse of multi-terminal devices was measured at wavelengths near 10 micrometers. It was found that these devices had interesting polarization-dependent photoresponse and could distinguish the incident polarization including circular from horizontal and vertical linear polarization. The devices also had photoresponse that depended on the incident angle of the illumination and the position of the illuminating spot on the device active region. Technical manuscripts describing this work were written and submitted to refereed journals. Interactions continued with colleagues in academia, industry, and at Air Force Laboratories.

Objectives:

The research objectives of this program were to fabricate optoelectronic devices and circuits from Weyl semimetals, and investigate their performance in terms of topologically-protected Weyl fermion interactions. The aim was to evaluate the suitability of Weyl devices for on-chip communications circuits. The possibility of significant improvements, compared to non-topological (i.e. conventional) materials, was explored by a series of electrical, optical, and magnetic measurements. The results may be of strong interest to the Department of Defense, and particularly the Air Force.

Approach:

The technical approach was to: (1) obtain crystals of Weyl semimetals including $MoTe_2$, WTe_2, and near-zero gap GeSn alloys with high Sn content, which may also be a possible candidate; (2) fabricate multiterminal device structures having contact electrodes that permit electrical, optical, and magnetic probing; (3) measure the characteristics and limitations of these devices under different conditions of current and voltage bias, and long-wave infrared illumination over a range of linear and circular polarizations; and (4) analyze, evaluate, and report their operation in terms of possible Weyl fermion transport mechanisms.

Motivation:

Weyl fermions were predicted theoretically in 1929, but were not observed until 2015 in families of materials know as Weyl semimetals including TaAs, NbAs, $MoTe_2$, WTe_2, and Mn_3Sn, and the list is growing daily. Weyl semimetals have topological properties that are

robust against defects, with extremely high values of charge carrier velocities and mobilities, as well as large nonlinear optical coefficients. Weyl fermions are massless and chiral, with their spin locked along the direction of velocity (right-handed), or against it (left-handed), thereby reducing scattering. Interestingly, the device and circuit capabilities of Weyl fermions may enable new levels of performance, but are only beginning to be explored, which is the subject of this current research program. Practical applications may include more rapid chipscale communications, sensitive far-infrared/terahertz interactions, and high-speed, low-power circuits.

Scientific Accomplishments:

During the fourth year of this project, multi-terminal devices were fabricated from several materials with near-zero energy bandgap. These devices were investigated, particularly regarding how their electrical characteristics were modified during illumination by various polarizations at long infrared (IR) wavelengths near 10 μm. The investigated materials included $Ge_{1-x}Sn_x$ alloys with high Sn contents, and some known Weyl semimetals including $MoTe_2$, and WTe_2, which were purchased (from *hq graphene*, The Netherlands). While awaiting the delivery of the Weyl semimetals, electrical and optical measurements were performed on the GeSn alloys, in part to determine if they exhibited exotic behavior, and in part to establish the experimental conditions and setups that would be subsequently used on the Weyl semimetals.

(a) Photoconductivity of low energy bandgap Germanium Tin alloys with up to 31% Tin

For sufficiently high Sn contents, above about 27 atomic percent, $Ge_{1-x}Sn_x$ alloys are predicted to have a zero bandgap, and may become a Dirac semimetal for somewhat higher Sn contents [H.-S. Lan, S.T. Chang, and C.W. Liu, Phys. Rev. B **95**, 201201 (2017)]. To investigate the possibility of exotic and Weyl fermion effects, a series of epitaxial $Ge_{1-x}Sn_x$ alloys with tin concentrations up to 31% (x=0.31) were grown by molecular beam epitaxy at relatively low substrate temperatures (down to 100 °C) using an electron beam Germanium effusion source, which gave similar material quality to alloys grown with a thermal effusion source, but at higher growth rates and with less unintentional hearing of the substrate. The GeSn films were characterized structurally by high-resolution X-ray Diffraction (XRD) and atomic force microscopy (AFM). GeSn photoconductor devices were prepared using standard Clean Room processing, and their optical response was measured by Fourier Transform Infrared Spectroscopy (FTIR) in the mid-infrared, and by using a variable wavelength quantum cascade laser in the long-wave infrared from 8.6 μm to 10.3 μm.

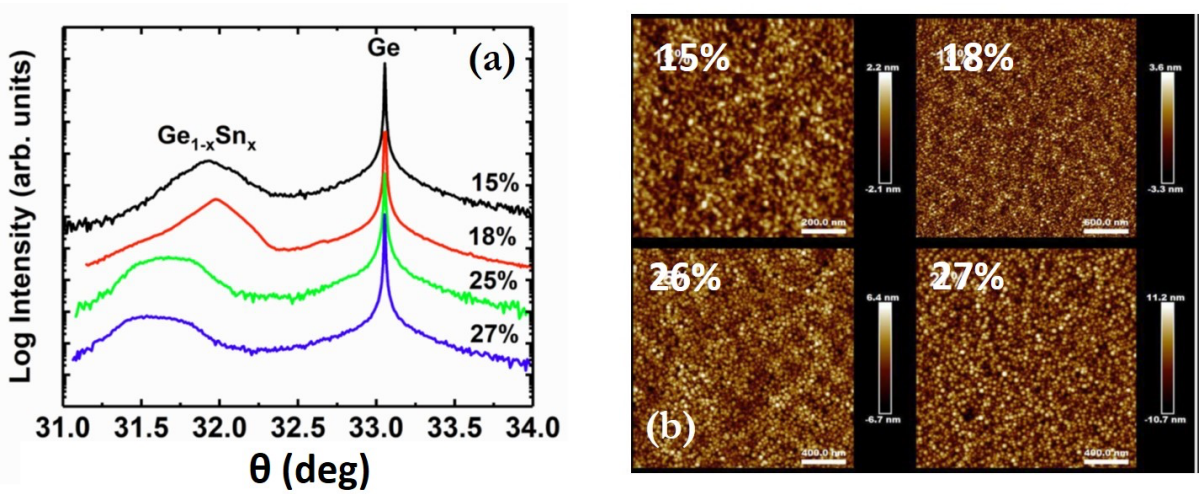

Figure 1. $Ge_{1-x}Sn_x$ structural and surface characterizations (a) high resolution X-ray diffraction (XRD) intensity versus scattering angle θ, showing the Ge substrate peak at 33.1 degrees, and the GeSn alloy peaks from 31.5 to 32 degrees, indicating increasing lattice constant with Sn content. (b) atomic force microscopy (AFM) scans versus composition for GeSn alloys. The scanned region was ~30×30 μm², and the surface height was less than 4 nm, indicating reasonably smooth layers. Note that the sample labeled 25% Sn in (a) and 26% Sn in (b) is the same sample, with the same Sn content within experimental error.

The $Ge_{1-x}Sn_x$ thin film samples were patterned into Van der Pauw devices and with interdigitated finger contact devices, as shown in Fig. 2(a) and (b), using standard photolithography and inductively coupled plasma (ICP) etching. The size of the device active region was 500 μm × 500 μm. For measurements, Beryllium-Copper spring clip electrodes directly contacted the outer region of the Van der Pauw pattern as in Fig. 5(a).

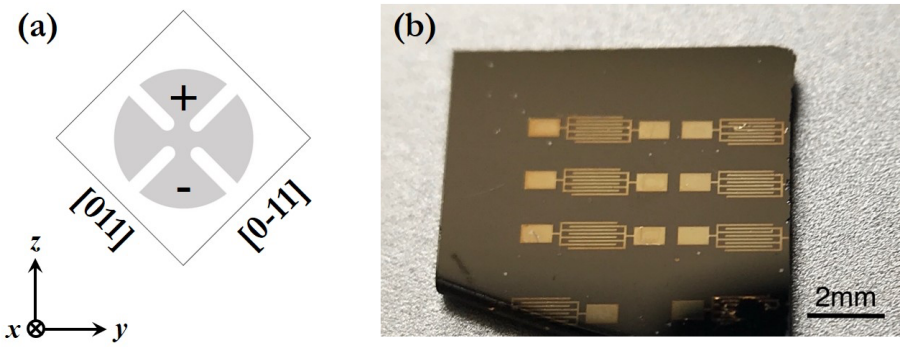

Figure 2. (a) Diagram of a $Ge_{1-x}Sn_x$ device indicating the crystalline directions. The active area was 500 μm × 500 μm. (b) Interdigitated finger contacts on a $Ge_{1-x}Sn_x$ photoconductivity device. The metallic contact pads were 1μm thick Ti/Pd/Ag, and the active area was 1700 μm × 750 μm.

To measure photoconductance, a tunable quantum cascade laser (Pranalytica OmniLux) emitting at wavelengths from 8.5 μm to about 10.6 μm was used as the infrared source, as in Fig. 3(a). A zero-order CdSe tunable (1-19 μm) quarter-waveplate (QWP), and half-waveplate (HWP) manipulated the polarization of incident beam. To avoid overheating, a neutral density (ND) filter was placed after the QWP/HWP to reduce the incident power on the $Ge_{1-x}Sn_x$ devices. A Ge Plano-Convex lens with a focal length of 100 mm was used to focus the beam onto the device active region.

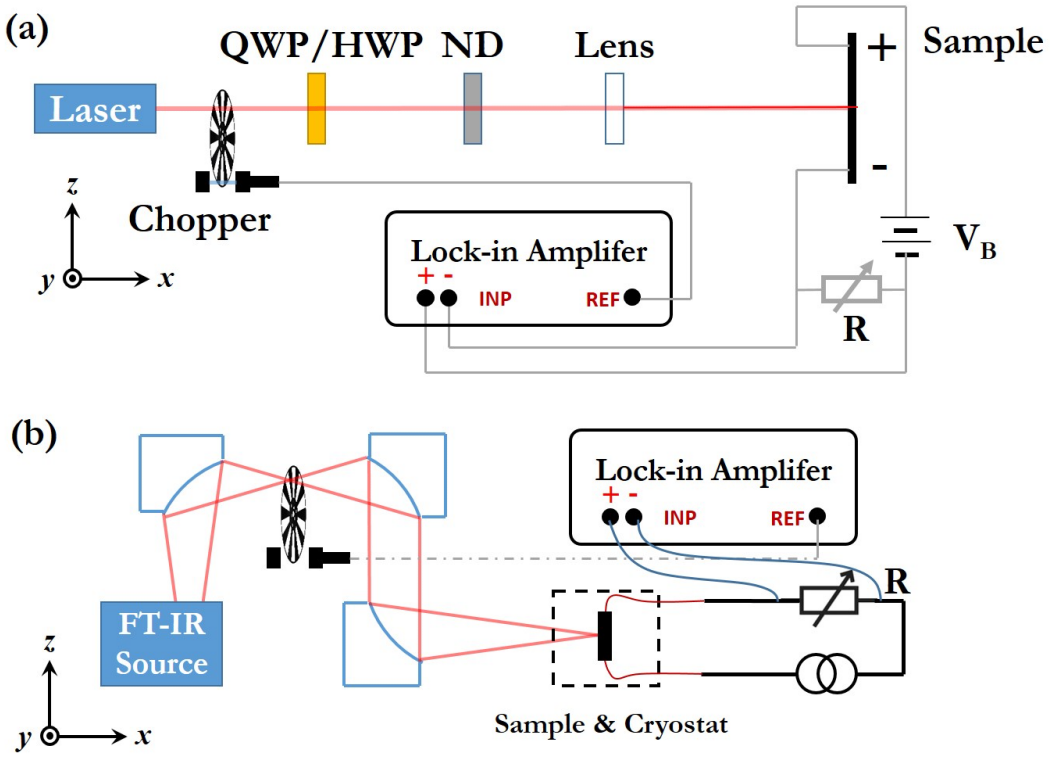

Figure 3. **(a)** Laser photoconductance setup. A quantum cascade laser at wavelengths from 8.5 μm to about 10.6 μm was used for illumination, with quarter-wave/half-wave plates (QWP/HWP), and neutral density filter (ND). The Lock-in amplifier measured the change in voltage induced across a resistor R placed in series with the illuminated device-under-test. **(b)** Fourier transform infrared (FTIR) spectroscopy setup for the optical absorption measurements of $Ge_{1-x}Sn_x$ devices.

Optical absorption and photoconductance measurements of $Ge_{1-x}Sn_x$ devices with tin content up to 31%, at wavelengths from 2 to 8 μm were made using a Thermo-Nicolet iS50R Fourier Transform Infrared (FTIR) Spectrometer system. As shown in Fig. 3(b), the collimated infrared source from the FTIR system was directed onto a two-inch parabolic mirror. A chopper wheel was placed at the focal point of the beam with a reference frequency of 509 Hz. Two additional parabolic mirrors focused the modulated beam onto the $Ge_{1-x}Sn_x$ "interdigitated finger" devices. For photoconductivity measurements, a current-bias circuit (I_{Bias} = 50 mA) shown in Fig. 3(a) was used to maximize the signal power transfer, and the synchronized (chopped) photocurrent signal was measured by a lock-in amplifier.

To account for the non-uniform optical intensity over the illumination spectrum, the FTIR was normalized to the flat spectral response of its internal deuterated triglycine sulfate (DTGS) detector. As shown in Fig. 4(a), the 21% Sn sample shows absorption out to about 7.5 μm. As a comparison, the absorption of $Ge_{0.82}Sn_{0.18}$ and $Ge_{0.85}Sn_{0.15}$ reached up to about 6 μm and 4 μm, respectively. Devices with greater than 21% Sn were not easily measured by the FTIR system, due to its relatively weak incident power at longer wavelengths. Instead, a quantum cascade laser (QCL) was used to measure $Ge_{1-x}Sn_x$ device photoconductance at wavelengths from about 8 μm to 10 μm, as shown in Fig. 4(b) and (c).

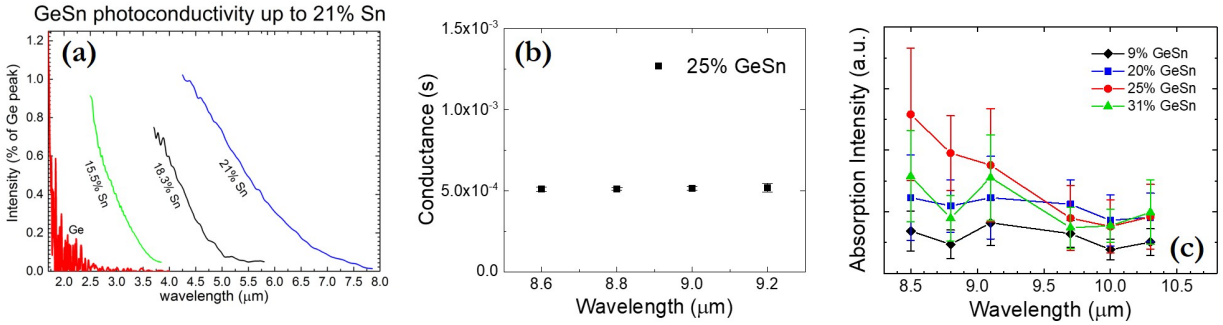

Figure 4. **(a)** The photoconductivity of three $Ge_{1-x}Sn_x$ films with Sn contents of 15.5%, 18.3% and 21%, measured from 2 to 8 μm by FTIR. Also included is the normalized response of a pure Ge sample (on Si substrate) as shown on the bottom left, which is weak out to about 4 μm. **(b)** For greater than 20% Sn, the photoconductance was measured by the change in photovoltage and photocurrent using a QC laser for several different wavelengths from 8.6 to 9.2 μm, showing relatively flat response. **(c)** Data of $Ge_{1-x}Sn_x$ optical absorption in the range from 8.5 μm to 10.3 μm. Although the absorption of the 25% Sn device is higher at 9 μm, the 31% Sn has the highest absorption at 10.3 μm.

We performed photoconductance measurements of a series of $Ge_{1-x}Sn_x$ thin-film devices with tin contents of 9%, 21%, 25% and 31%. The spectral photocurrent I_{ph} was related to the corresponding optical absorption α using the equation:

$$I_{ph}(h\upsilon) = \frac{q\eta P\tau_L(\mu_n+\mu_p)Wd^2V_{Bias}}{h\upsilon * l}\alpha(h\upsilon) \qquad (1)$$

where q is the electronic charge, η is the quantum efficiency, P the incident power, and τ_L, μ_n and μ_p are the carrier lifetime, electron and hole mobilities, respectively; W, d, l indicate sample size, width, thickness and length, respectively, V_{Bias} is the applied voltage bias, h is Planck's constant, and υ is the photon frequency.

Using Eqn. (1), under normal incidence, the optical absorption of $Ge_{1-x}Sn_x$ devices was analyzed by measuring photocurrents at the infrared wavelengths from 8.5 μm to 10.3 μm.

The spectral absorption coefficient α was related to the bandgap energy using the Tauc expression:

$$\alpha \propto \frac{\beta}{h\upsilon}\left(h\upsilon - \left(E_g - h\vartheta\right)\right)^n \qquad (2)$$

where $h\nu$ represents the *photon* energy, and $h\vartheta$ is the optical *phonon* energy. E_g represents the bandgap energy, β indicates a material based constant, and the exponent n depends on the nature of the optical transition. For example, if n=1/2, the material has a bandgap that is direct in *k-space* ; for an indirect material, n equals 2.

The spectral absorption data for α versus photon energy $h\nu$ were used to construct Tauc plots that extrapolate to zero absorption at the bandgap energy. The absorption data revealed that the bandgap of $Ge_{1-x}Sn_x$ was *direct* in *k*-space, and decreased as the tin content increased from 9% to 31%. $Ge_{1-x}Sn_x$ was predicted to have a zero bandgap for tin content exceeding 27%, and therefore, the absorption should extend into the far IR. Using the Tauc approach for the 31% Sn device, however, we obtained a bandgap energy of 0.1 eV. For reasons that are not yet clear, this value was not zero (or negative) that was expected for this composition, but may suggest that either the Tauc method is invalid for zero or negative energy band semimetals, or that the GeSn alloys may have more complex behavior, such as the presence of short-range order (SRO), which is predicted to affect the band energies.

Based on these findings, including the significant photoconductive response, the high tin content $Ge_{1-x}Sn_x$ alloys were demonstrated to be good candidates for devices in the mid- and long-wave infrared regions, and suitable for Air Force applications. In addition, the possibility of exotic Dirac and Weyl behavior motivates continued study.

(b) Polarization and angle dependent long wave photoresponse of low energy bandgap GeSn devices

In addition to exhibiting photoresponse at long infrared (IR) wavelengths, it was found that the $Ge_{1-x}Sn_x$ optoelectronic devices were polarization sensitive. In a series of experiments, polarization-dependent and incident angle-dependent photocurrents were observed in $Ge_{1-x}Sn_x$ optoelectronic devices with Sn fractions from x = 0.09 to x = 0.31, under illumination in the long-wave IR region from 8.8 μm to 10.6 μm. This behavior was observed both with and without applied voltage bias. The photoresponse *increased* as the polarization was changed in a sequence from vertical-linear, to circular, to horizontal-linear. Data analysis suggested that this dependence was due to Fresnel reflection and transmission, and to the different absorbance between the polarizations at oblique angles of incidence. This finding demonstrated an interesting mechanism for incident polarization and angle-detection for long-wave infrared applications.

The $Ge_{1-x}Sn_x$ alloy films with different compositions were deposited on 700 μm thick Ge (100) substrates and on undoped semi-insulating GaAs (100) substrates by the method of

molecular beam epitaxy (MBE). X-ray diffraction indicated that the films had thickness above 100 nm with high uniformity, and were of high crystalline quality with a face-centered cubic structure. The films were largely relaxed (film relaxation > 90%) for Sn fraction $x > 0.18$, and had an *rms* surface roughness below 3 nm, determined by atomic force microscopy (AFM).

Photolithography and inductively coupled plasma (ICP) etching were used to pattern the $Ge_{1-x}Sn_x$ thin films into optoelectronic devices, as shown in Fig. 5. Electrical contacts were patterned along the <100> directions, as shown in Fig. 5(a). An SEM image of a typical $Ge_{0.69}Sn_{0.31}$ device is shown in Fig. 5(b). In all the experiments, beryllium-copper (BeCu) spring clips directly contacted the outer regions of the devices with no other intervening metal.

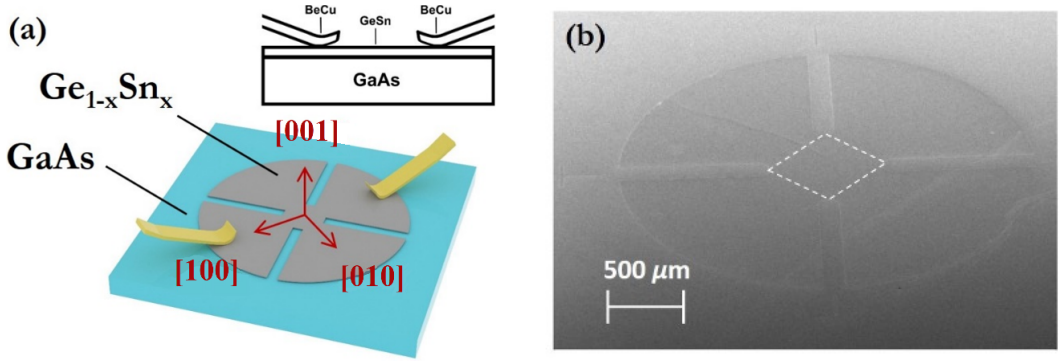

Figure 5. (a) Diagram of a $Ge_{1-x}Sn_x$ device indicating the crystalline directions with respect to the four contact regions. Two BeCu clamps were placed on a pair of contacts along the [100] direction. **(b)** SEM image of the $Ge_{0.69}Sn_{0.31}$ device; the size of its central region is 500 μm × 500 μm (white dashed-line enclosed area).

To investigate the infrared photoresponse, we utilized an 8.8 μm wavelength quantum cascade laser (Pranalytica OmniLux), and a 10.6 μm CO_2 laser, as shown in Fig. 6. For vertical/horizontal linear polarization, we used a 1–19 μm broadband zero-order tunable half-waveplate (HWP); and for vertical linear & right/left circular polarization, we used a quarter-waveplate (QWP) (ALPHALAS CdSe). Before each measurement, the incident laser power was varied by the neutral density filter (ND) to between 12 to 15 mW, as recorded by two power meters. The oblique incident angle θ of the device illumination direction was varied from zero (normal incidence) to 60°. The polarization phase angle φ was defined as the angle between the optic component's fast axis (QWP, HWP, or polarizer) and the vertical z-axis direction as in the Fig. 6 inset. For the CO_2 laser, the polarization was manipulated by a reflective phase retarder and a polarizer.

A longitudinal measurement geometry (Fig. 6) was used, and the induced photocurrent was in the plane of incidence along the [100] direction of the device (as in Fig. 5), and indicated by the + and – signs in Fig. 6. The photocurrent was measured by the lock-in technique working in the low input impedance "current mode", to obtain the short-circuit current for the cases of no applied current or voltage bias. The light chopper reference frequency was

219 Hz. The infrared beam was varied from linearly vertical ***p***-polarized (|| z axis), to left- and right-handed circular polarization (LCP/RCP) by rotating the QWP angle φ.

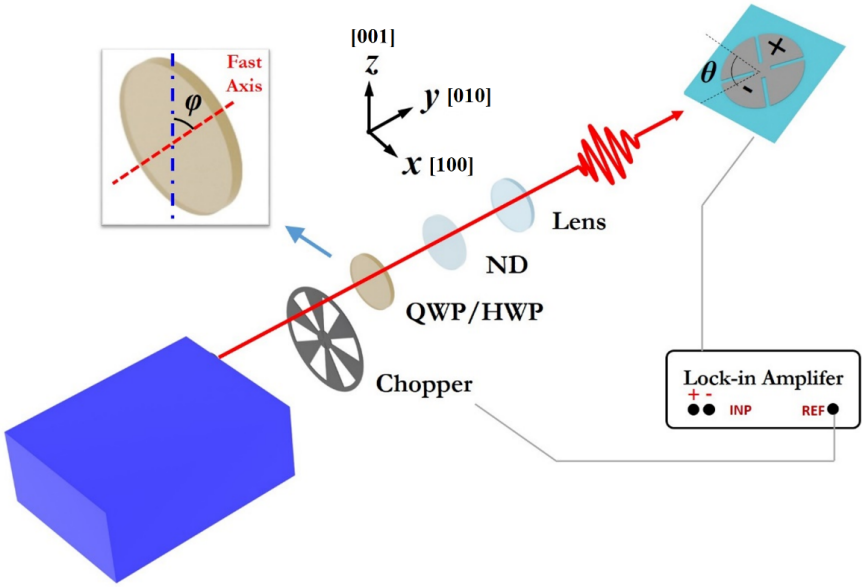

Figure 6. Polarization and incident angle dependent photocurrent measurement setup and device geometry, showing quantum cascade laser (QCL) to the left with either a quarter-wave plate (QWP) or a half-wave plate (HWP), and neutral density filter (ND). A Ge Plano-Convex lens with a focal length of 100 mm was used to reduce any variation in position of the illuminating spot on the GeSn device (at the right). The device under test was mounted on a stage with an incident angle θ between the device surface normal and the incident direction of IR laser excitation (*measurement* y-axis). The inset shows the polarizer angle φ, defined as the angle between the polarizer fast axis and the vertical direction (*measurement* z-axis). The Lock-in signal (INP) and frequency reference (REF) inputs are labeled. Note that the x,y,z coordinate system shown here refers to the *measurement* apparatus, and differs from the *device* coordinates used in Fig. 5.

As shown in Fig. 7(a), for the incident angle θ = 60°, the photocurrent attained its maximum for the LCP and RCP with (QWP angles φ=45° and 135° respectively), but was at a minimum for the vertical linear (***p***) polarization (|| z axis, at QWP angles: 0, 90 and 180 degrees). The measured photocurrent was normalized by its corresponding *incident* power, measured with a broadband power meter. In this study, the powers *reflected* from the device were *not* taken into account. The difference in the normalized photocurrent responses for right-hand and left-hand circular polarization was not considered significant. In all cases, the amplitude of the photoresponse increased with the Sn content, although for the 20% Sn device, the variation of current with polarization appeared relatively strong.

The quarter wave plate used in Fig. 7(a) was unable, however, to produce *horizontal* (***s***) linear polarization. To check for the response versus the direction of *linear* polarization, we

utilized a half-waveplate to rotate the laser linear polarization, and the measured photocurrent response is shown in Fig. 7(b). The polarization ranged from vertical ***p***-polarized (HWP angles of 0, 90 and 180 degrees) to the horizontal ***s***-polarized direction (HWP angles of φ=45° and 135°). The photocurrent reached a maximum at the horizontal linear polarization, and a minimum at the vertical linear polarization, similar to Fig. 7(a). This polarization dependence was analyzed to determine underlying physical mechanisms.

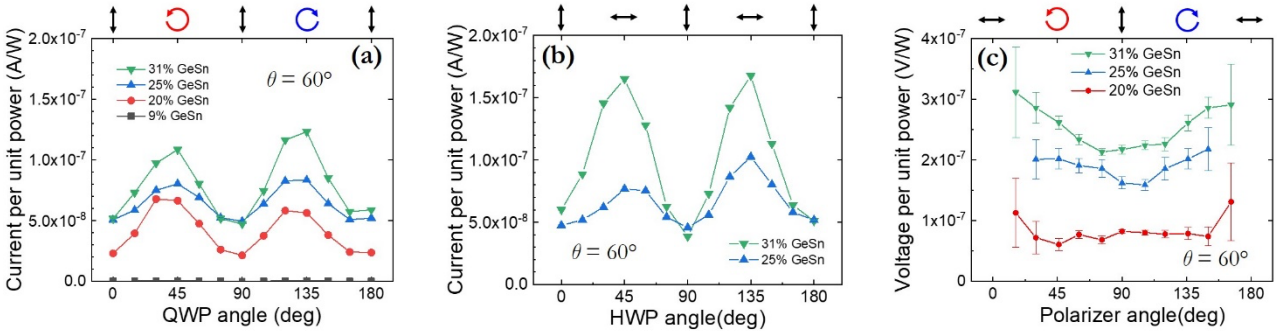

Figure 7. Photocurrent response of the $Ge_{1-x}Sn_x$ devices, showing the effects of linear and circular polarization. The horizontal axes indicate the angle φ between the polarizer axis and the vertical direction, which varied the polarization from linear to circular, as indicated along the top of the plots. The symbols show whether the polarization was vertical linear (↑), horizontal linear (→), or left (↺) or right (↻) circular. In all cases, the current was measured along the longitudinal [100] axis of the device, which is along the direction of the incident light. **(a)** photocurrent at 8.8 μm wavelength normalized to incident power versus polarization as controlled by the *quarter-wave plate* (QWP). **(b)** normalized photocurrent versus horizontal and vertical linear (*only*) polarizations, controlled by the *half wave plate* (HWP), for two of the devices measured in (a). **(c)** Normalized photovoltage measured using a 10.6 μm *CO_2 laser* with a reflective phase retarder yielding vertical, horizontal, and circular polarizations. The Sn content of the detectors is indicated. In plots (a) and (b), the error bars were smaller than the symbol size. All experiments were performed at room temperature. Note that in all cases, the vertical linear polarization gave the weakest response.

In all cases, the photoresponse signal amplitude increased with increasing Sn content. In Fig. 7(a), the GeSn device with 9% Sn showed negligible photocurrent response, presumably because the incident photon energies were below the bandgap absorption edge of this sample., The incident light energies were 0.141eV at the wavelength of 8.8 μm, and 0.117 eV at 10.6 μm, whereas the calculated bandgap of $Ge_{0.91}Sn_{0.09}$ was 0.490 eV according to theory, so it was reasonable that this device had no photoresponse. For comparison, the $Ge_{1-x}Sn_x$ bandgaps for x=0.25 and 0.31 are expected to be below the incident photon energies, and these wavelengths were in fact absorbed. An interesting exception is the x=0.20 sample, which showed response at both wavelengths (weakly at 10.6 μm), although its expected bandgap is 0.169 eV, which lies *above* the photon energies.

It may be that the actual bandgap energy of the x=0.20 sample was in fact near or below 0.117 eV, but this has not yet been established.

As shown in Fig. 8, the dependence of the photoresponse on polarization occurred only at *oblique* incidence, for example at θ = 60° and 30°. There was no polarization dependence at θ = 0° (normal incidence). The polarization response data of Fig. 8(a) was analyzed according to the functional dependence on the polarizer angle φ and incident angle θ (per Fig. 6). The induced photocurrent response ***j*** followed:

$$j(\theta, \varphi) = D(\theta) + L_C(\theta) \cos 4\varphi \qquad (3)$$

where $D(\theta)$ identifies a component independent of polarization, and $L_C(\theta) \cos 4\varphi$ denotes the contribution from polarized light. A functional analysis for the special case θ = 60° yielded D(60°) = (6.56±0.04)×10^{-8} A/W, and L_C(60°)= (1.67±0.06)×10^{-8} A/W. The increase in response with incident angle θ followed a trend expected from the differences in Fresnel reflections internal to the device for the ***s*** and ***p*** polarizations.

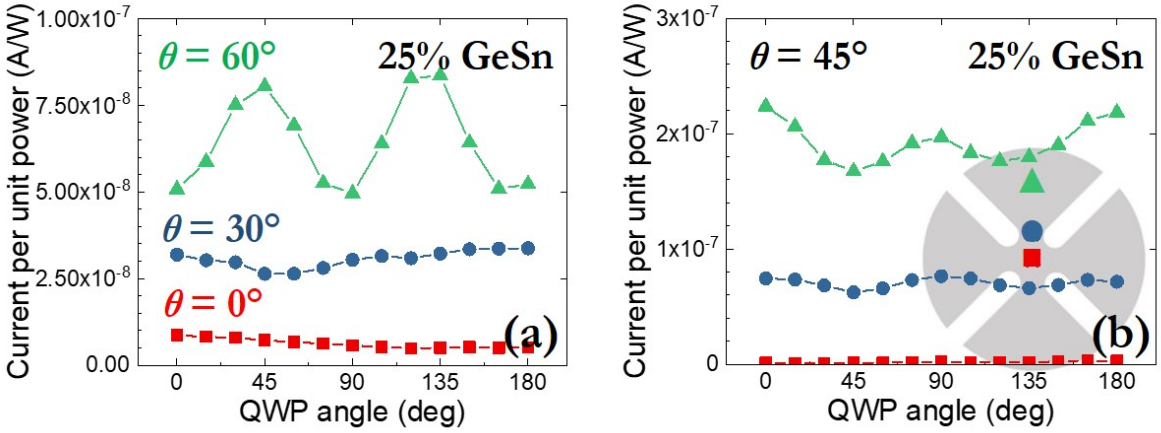

Figure 8. The dependence of the $Ge_{0.75}Sn_{0.25}$ device photocurrent on polarization (QWP angle) and on illumination incident angle, and spot location. The QWP angles of φ=45° and 135° gave circular RCP and LCP, respectively, and QWP angles of 0°, 90° and 180° gave vertical linear polarization (***p*** polarization). Left panel **(a)** shows the increase of photocurrent with incident angle ***θ*** between the incoming beam and the device normal. The angles θ=0° (red), 30° (blue), and 60° (green), showed an increasing response with angle, with no signal at normal incidence θ=0°. Right panel **(b)** shows photocurrent versus position of the beam spot on the device. The highest photocurrent was for the triangle symbol where the spot was nearest the electrical contact, as shown in the inset; the circular symbol indicates when the beam spot was located near the edge of the central region. The photoresponse was negligible with the spot at the device center, shown by the square symbol.

The difference in absorption between vertical and horizontal linearly polarized light suggest that the Fresnel equations were likely the origin of the observed polarization

dependence, specifically, the $\cos 4\varphi$ term in Eq. (3). For light incident on the interfaces between air and $Ge_{1-x}Sn_x$, and between the GeSn and the substrate, which have different refractive indices, the corresponding reflectance and transmittance of the vertical and horizontal linear polarization components varied with incident angle. Under an oblique incident angle (θ = 60°), there was a path-dependent difference of total absorbance for the two polarization components. Due to Fresnel reflection at the interfaces, more of the incident horizontal linear ***s***-polarization would be reflected back and forth into the GeSn layer from both interfaces, leading to larger net absorbance, and larger photoresponse compared to the vertical ***p***-polarization, which is less likely to reflect back into the GeSn active region. At *normal* incidence, as shown by the red curve in Fig. 8(a), θ=0°, the photocurrent was greatly reduced and no polarization dependence was observed, since there is no difference in the reflectivity (and hence absorbance) of the different polarizations. The reason for the overall low response signal level at normal incidence, however, was unclear. Due to uncertainties in the precise wavelength dependent values of the refractive index in each material, a quantitative calculation of the Fresnel response was not yet performed.

The amplitude of the photoresponse signals also varied with the *position* of the illumination spot on the devices, with the strongest photoresponse observed when the spot was focused near an electrical contact, marked as the triangle symbol in Fig. 8(b). The response was significantly reduced when the spot was moved to the *center* of the devices. It was also noticed that the photocurrent reversed sign at the opposite contact suggesting that the zero-bias photoresponse is associated with a contact effect, such as a metal-semiconductor junction, or with the preferential heating (thermo-electric effect) of the illuminated contact. Secondly, we observed that the response increased with greater incident angle away from the normal, as expected from an increase in optical absorption because of the longer light path with angle. Thirdly, for the semi-insulating GaAs substrate used in these experiments, there was negligible absorption in the long wavelength infrared region because the substrate has a direct absorption edge for interband transitions with a *long wavelength* cutoff of around 0.8 μm [ref: O. Madelung; and/or A. Dargys and J. Kundrotas], and therefore the substrate was not expected to contribute. We also measured the photocurrent under both current and voltage bias which gave similar polarization dependency but with much a higher noise level than the *zero-bias* results shown here.

In summary, the polarization-dependent and incident angle-dependent long wavelength excitation response of $Ge_{1-x}Sn_x$ devices with Sn fractions x=0.09, 0.20, 0.25, and 0.31 in the active region were investigated. This long wavelength photocurrent response has seldom been reported for $Ge_{1-x}Sn_x$ group IV semiconductors, which hold promise for long-wave infrared applications such as remote sensing, environmental monitoring, medical diagnostics and thermal imaging. The origin of the photocurrent response was attributed to the difference of absorption between two linear polarization components (perpendicular and horizontal). From the perspective of applications in optoelectronic devices, these polarization and angle dependent properties could be applied for metrology applications at long-infrared wavelengths. We demonstrated that the $Ge_{1-x}Sn_x$ optoelectronic devices with high Sn concentrations, especially, x=0.25 and x=0.31, have higher photodetector sensitivity at the long-wave infrared wavelengths of 8.8 μm and 10.6 μm. It is interesting to

speculate that the $Ge_{1-x}Sn_x$ bandgap may decrease to near zero as the Sn content increased to 27%. It may be that $Ge_{0.69}Sn_{0.31}$ is a zero bandgap semimetal with a negative bandgap parameter $E_{gap} = -0.1$ eV, although the value of bandgap energy measured in Section (a) above (+0.1 eV)was *nonzero*. These results may be crucial for the design of $Ge_{1-x}Sn_x$ based optoelectronic devices in the future.

(c) Polarized Photoresponse of the Weyl Semimetal WTe_2

In addition to the narrow energy gap GeSn alloys, experiments were performed on the known Weyl semimetals, $MoTe_2$, and WTe_2, that were obtained commercially from *hq graphene*. Polarization-dependent device photoresponse was explored, using a setup and procedure similar to that shown in Fig. 6 for the GeSn devices, except that the figures below plot the *voltage* (not *current*) response. Note that for the constant current bias, a *smaller* voltage implies *greater* photoconductivity. A quarter-wave plate (QWP) was used to vary the incident polarization, and a power meter was placed above the sample to measure the reflected power if the incident angle was oblique. The wavelength of 9.5 μm was omitted from the measurements because of its lower power relative to the other wavelengths from the tunable Quantum Cascade Laser. A photograph showing the device current direction relative to the incoming light beam for these measurements is shown in Fig. 9.

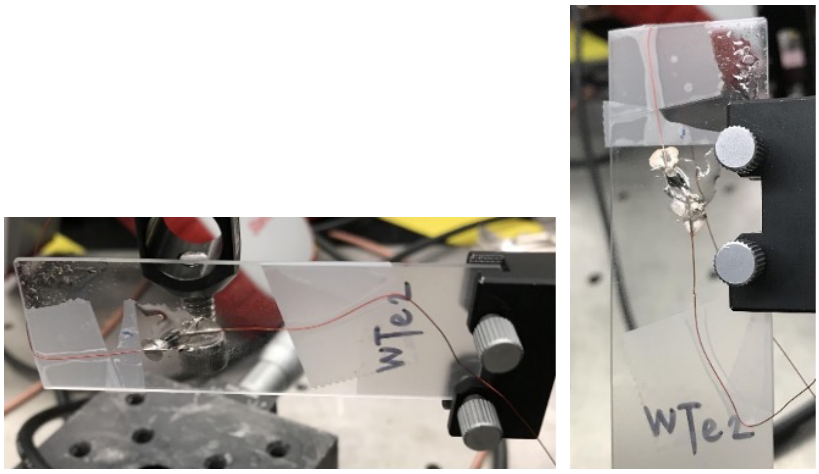

Figure 9: Photograph showing the orientation of the measured current direction of the device with respect to the incoming illumination (perpendicular to the plane of the photos). **(a)** Orientation of the device crystal for current *transverse* to direction of illumination. **(b)** Orientation of the crystal for current *along* the direction of illumination, and used for the results in Fig. 10. Because WTe_2 is a *Type II* Weyl semimetal, the orientation can influence the strength of the photocurrent. For this reason, these photos have been included to document this orientation for future reference.

The WTe_2 device had a polarization-dependent photoresponse that increased with the incident angle θ. After accounting for the variation of *reflected* power on θ, the polarization-dependent response persisted. As shown in Fig. 11, however, due to the reflected beam being scattered into a line instead of remaining as a point, the power meter

may not have been able to measure the entire reflected power, and the actual "corrected" signal strength may be *higher* than plotted below.

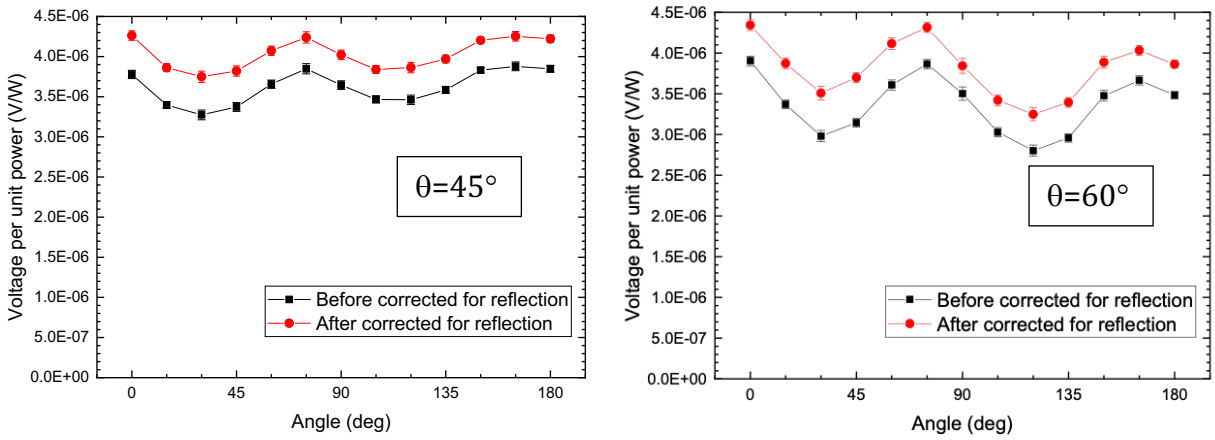

Figure 10: Dependence of WTe_2 device photovoltage on polarization (QWP angle φ), and illumination angle of incidence *θ*. The QWP angles φ=45° and 135° gave right hand circular (RCP) and left hand circular (LCP), respectively; and QWP angles φ= 0°, 90° and 180° gave *vertical* linear ***p*** polarization. The measured current direction was along the incident beam as shown in Figure 9(b). Note that for a constant current bias, a *higher* voltage implies *higher* resistance and *lower* photoconductance. Therefore a lower voltage implies greater device photoresponse. Left panel **(a)** shows polarized photovoltage results pertaining to the WTe_2 device at ***θ=45°*** *incidence* accounting for reflected power. Right panel **(b)** shows polarized photovoltage for WTe_2 at *60° incidence*, with slightly greater polarization dependence. For both angles of incidence, the device photoresponse is greater for circular polarization (lower voltage). Note that the actual voltage per power may be higher than plotted here, as explained in Fig. 11, because the reflected power may be greater than measrued.

As shown in Fig. 10, the photoresponse of the WTe_2 Weyl fermion device showed strong dependence on incident polarization. As explained in the Fig. 10 caption, the *smaller* voltage per power signal that occurred for circular polarization at the QWP phase angles of 45° and 135° were associated with *larger* photoconductance, and hence greater generation of charge carriers by the incident light. These results show that the WTe_2 device may be used as a polarization detector, and as an incident angle detector. It is not yet clear if the polarization dependence was due to the selection rules caused by Weyl fermion absorption, or more conventionally, to the difference in absorbed light due to Fresnel reflections at device internal interfaces. This behavior is worthy of further study, and suggests that Weyl fermion devices may be useful for Air Force applications in the long-wave infrared regime.

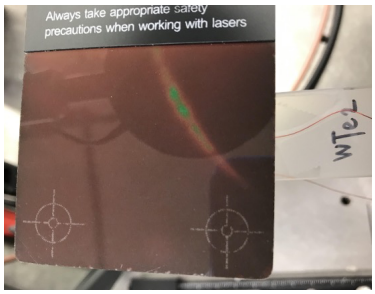

Figure 11: Photograph of laser light pattern incident on an infrared detector card that was placed as close as possible to the WTe_2 device location. Here, the discovery was made that the incident beam was not a single point, but rather a green curved streak shown on the upper right portion of the card. The power meter cannot capture all of this beam, which may have caused the measured *reflected* power that was used to correct the results shown in Fig. 10 to be *lower* than it actually was. Therefore the power absorbed by the device may be smaller than indicated and hence the actual normalized response may be *higher* than shown in Fig. 10.

(d) Technical Interactions

During the course of this project, the productive interactions with colleagues in academia, industry, and government laboratories continued.

Discussions and meetings were held with Dave Beatson, general manager of Thorlabs Quantum Electronics (Jessup, MD), regarding infrared detectors and instrumentation. Thorlabs made contributions of optical components that assisted our experiments.

Discussions and meetings were held with Prof. Pinaki Mazumder of the University of Michigan, about Weyl device theory, modeling, and simulation, and joint research collaborations.

Meetings were held with Prof. John Xiao, Dept. of Physics & Astronomy, University Delaware about materials, magnetic measurements and device theory. Prof Xiao provided samples of Mn_3Sn, an antiferromagnetic Weyl semimetal, for optoelectronic measurements.

Discussions continued with Prof. Stefan Zollner, New Mexico State University, about GeSn characterization via spectroscopic ellipsometry, which gives information about the energy band structure. Two papers were published in refereed journals about the energy band properties of GeSn alloys.

Interaction continued with Dr. Dominic Imbrenda, a former student, and now project manager at the Lockheed-Martin Research Lab in Cherry Hill, NJ. Dominic's collaboration is encouraged by Lockheed-Martin upper management, and he spent several days in our lab measuring the optical characteristics of devices.

Discussions continued with colleagues at AFRL in Dayton, OH; particularly with Drs. Chip Claflin and Arnold Kiefer, regarding GeSn alloys and the properties of Weyl fermions.

Significance, Relevance and Importance:

For almost a decade, Weyl semimetals and Weyl fermion excitations have exhibited remarkable electrical and optical properties that are compelling for practical applications of interest to the Air Force. The research performed during the course of this research program showed that electrical and optical devices fabricated from low energy bandgap materials including GeSn alloys and several Type-II Weyl semimetals can distinguish between the polarizations and incident angel of long-wave infrared illumination. These findings are important for fundamental science and practical commercialization, and strongly suggest further study.

Novelty:

The novelty of this research program is compelling because Weyl semimetals were unavailable prior to the year 2015. Since then, the list of Weyl semimetals has grown considerably, and the properties are exotic and fascinating. The research performed in this program demonstrated that optoelectronic devices that are polarization- sensitive, incident angle-sensitive, and position-sensitive can be fabricated with operation in the long-wave infrared regime that is important for military and commercial applications.

Publications (submitted, accepted, published); Presentations:

Dominic Imbrenda, Rigo A. Carrasco, Ryan Hickey, Nalin S. Fernando, Stefan Zollner, and James Kolodzey, "Band Structure Critical Point Energy in Germanium-Tin Alloys with High Tin Contents," *Appl. Phys. Lett.*, 119(16), 162102 (2021); https://doi.org/10.1063/5.0064358

Tao Wang, Calvin Duong, Dominic Imbrenda, Ryan Hickey, Benjamin Garrett, Mark Mirotznik, and James Kolodzey, "Polarization and angle dependent long wavelength photoresponse of GeSn devices with high tin concentrations," *Optics Express*, (2019), submitted.

Tao Wang, Calvin Duong, Ryan Hickey, Dominic Imbrenda, and James Kolodzey, "Infrared photoconductivity of germanium tin alloys with up to 31% tin," (2019), manuscript in preparation.

Guangyang Lin, Peng Cui, Tao Wang, Ryan Hickey, Jie Zhang, Haochen Zhao, James Kolodzey, and Yuping Zeng, "Fabrication of germanium tin microstructures through inductively coupled plasma dry etching," IEEE Trans. on Nanotechnology, 2021, in press.

Ryan Hickey, Dominic Imbrenda, and James Kolodzey, "Low temperature molecular beam epitaxy growth of germanium tin alloys with up to 31% tin," (2019), manuscript in preparation.